Clean Process to Utilize the Potassium-Containing Phosphorous Rock with Simultaneous HCl and KCl Production via the Steam-Mediated Reactions

Yunshan Wang, Lufang Shi, Houli Li, Yixiao Wang, Zhiying Wang, Xuebin An, Mingzhu Tang, Gang Yang,* Jun He, Jing Hu, and Yong Sun*

ACCESS | 📊 Metrics & More | 📰 Article Recommendations | 🆂🅸 Supporting Information

ABSTRACT: In this paper, a clean process based on the steam-mediated reactions for simultaneous HCl and KCl production using the potassium (K)-containing phosphorous rock as a precursor is proposed. Through hydrochloric acid (HCl) leaching, not only the generation of H_3PO_4 and $CaCl_2$ (via further precipitation) were realized but also the acid-insoluble residue [phosphorous-rock slag (PS)] rich in elements, that is, K, Al, Si, and so on, in the form of microcline ($KAlSi_3O_8$) and quartz (SiO_2) was obtained and became readily available for further HCl and KCl generation. Over 95% of the elements, that is, K, Al, and Si, come into the final products, and the overall acid consumption (based on HCl) is significantly reduced (90%) due to recovery of acids. The impacts of the key operational parameters such as temperature, duration, and reagent impregnate ratio were rigorously analyzed via a supervised machine learning approach, and the optimal conditions were determined [reaction temperature, X_1, 850 °C; reaction duration, X_2, 40 min; and impregnate ratio (PS over $CaCl_2$), X_3, 2.5] with approximately ±10% uncertainties. Thermodynamic analysis indicates that the introduction of steam to PS + $CaCl_2$ not only enhances the chemical potential for the formation of HCl and KCl but also provides the transport advantage in continuously removing the generated products, that is, HCl and KCl, out of the system. Molecular simulation indicates that the presence of both steam and SiO_2 in the PS matrix plays critical roles in decomposing PS + $CaCl_2$ at high temperature. The shrinking core model shows that both the intrinsic kinetics and transport are influential with the activation energy being around 14.63 kJ/mol. The potential reaction pathway is postulated.
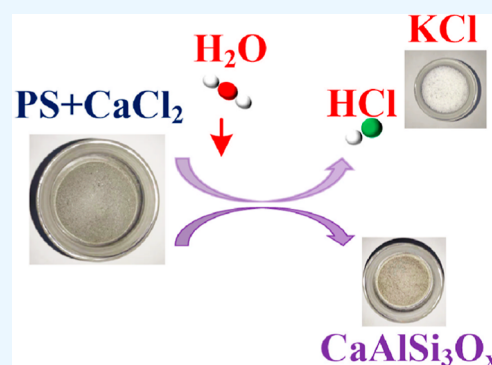
1. INTRODUCTION

Food security is paramount to the countries with a large population.[1] The productivity of major crops relies on the sufficient supply of nutritional elements such as phosphate (P) and potassium (K). The common practice of obtaining P and K elements derives from metallurgical processes using different sources, that is, phosphorous rock (PR) and potash.[2,3] In China, the sedimentary phosphorous deposits are one of the main resources for extracting the useful P derivate to produce phosphorous fertilizers and phosphoric acid (H_3PO_4).[4,5] Most phosphate fertilizers and H_3PO_4 are produced through a so-called wet process (or the dihydrate process), in which the ternary acidic system of $H_2O-H_2SO_4-H_3PO_4$ is used as the leaching medium and its byproduct $CaSO_4·2H_2O$ (gypsum) is largely produced.[6] The inherent drawback of this conventional process lies in the continuous consumption of the acid (H_2SO_4) and accumulation of the byproduct gypsum.[7] When the sulfate ion (SO_4^{2-}) migrates from sulfuric acid (H_2SO_4) to gypsum ($CaSO_4·2H_2O$), it creates a great challenge for recovering the sulfuric acid in the aspect of energy consumption at high temperature.[8,9] In other words, the decomposition of calcium sulfate ($CaSO_4$) back into the base

and acid is an adverse thermodynamic barrier to overcome.[10] To make the situation even worse, this conventional wet process also shows poor performance in effective utilization of the residues (i.e., K, Ca, Al, Mg, Si, etc., more than 60 wt % becomes waste slag).[11,12] For example, the waste slag often ends up with stockpiling as phosphorous gypsum in colossus amount, posing a great hazard to the local environment, such as the great potential hazard made by stockpiling of phosphorous gypsum at the Yangzi River region.[13,14] Depending on the originality, the primary mineral matrix of the phosphorus rock (PR) varies significantly.[15] Taking the PR from southwest China as an example, the primary mineral matrix in PR often includes the fluoroapatite groups ($Ca_5(PO_3)_3F$), dolomite ($CaMg(CO_3)_2$), microcline (KAl-
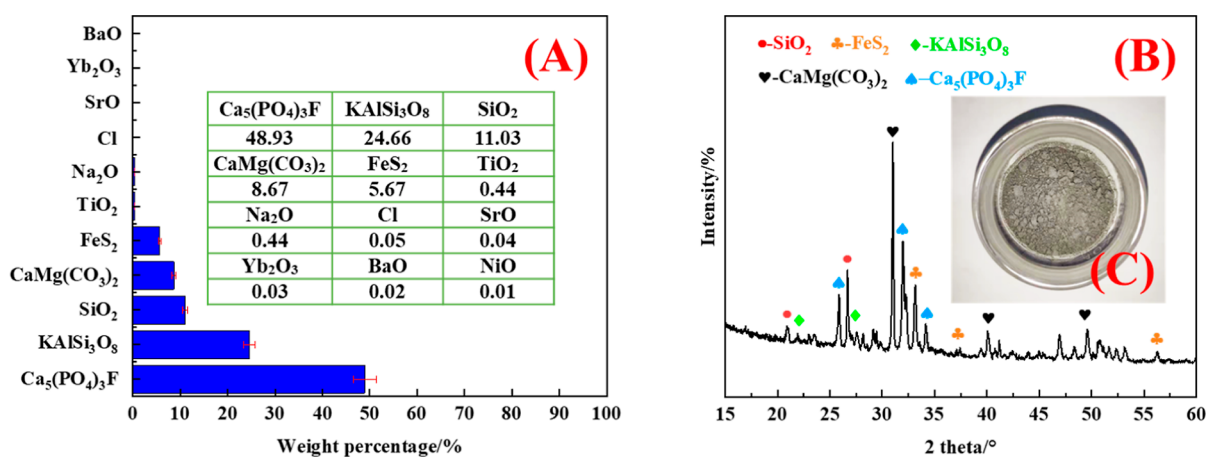
Figure 1. Characterization of PR: (A) XRF analysis of the main compositions in PR within ±10% uncertainties, (B) XRD, and (C) photo image of PR.
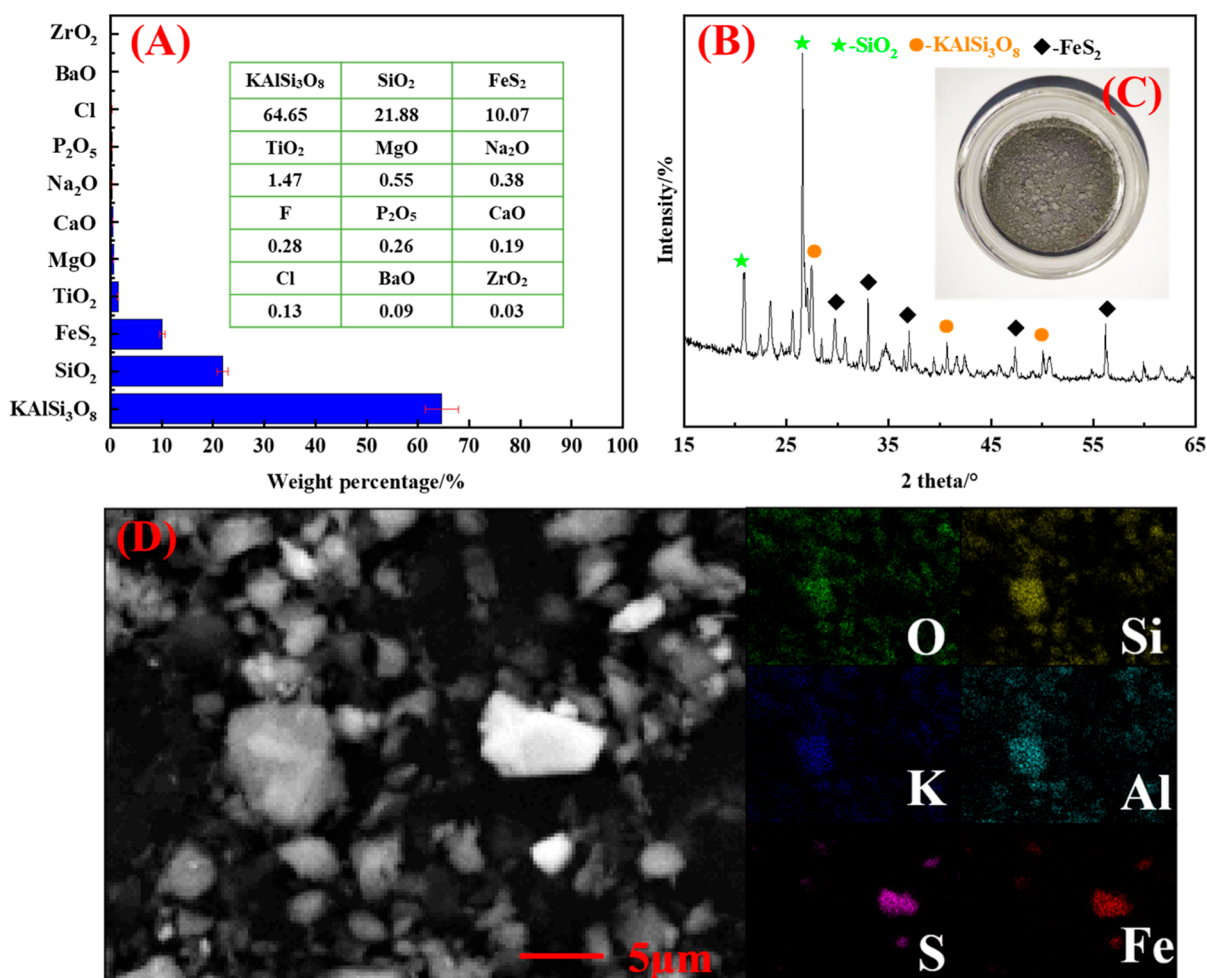

Figure 2. Characterization of phosphorous-rock slag (PS): (A) XRF analysis of the main compositions in PS within ±10% uncertainties, (B) XRD, (C) photo image of PS, (D) and SEM−EDS mapping for the key elements in PS.

Si$_3$O$_8$), quartz (SiO$_2$), and so on. To overcome the problem that the conventional sulfuric acid-based wet process encountered during PR processing, a new process based on chloride ions (Cl$^-$) is developed in this work. The benefits of using hydrochloride acid (HCl) lie in the following reasons: (i) different reactivities between the minerals and acid, generating the acid-dissolving products and insoluble residues [phos-

phorous-rock slag (PS)] to separate, (ii) simultaneously generating and removing KCl from PS during the steam-mediated reaction, and (iii) relative easiness in recovering HCl through the addition of calcium chloride salts (CaCl$_2$) to the PS in the presence of steam at higher temperature. With regard to the reactivity during acid leaching, the acid-dissolving minerals, that is, fluoroapatite groups (Ca$_5$(PO$_3$)$_3$F) and

dolomite $(CaMg(CO_3)_2)$, will react with acids actively and dissolve into the leachate. The main products of H_3PO_4 and $CaCl_2$ (via further precipitation) are obtained, leaving acid-insoluble residues rich in elements, that is, K, Al, Si, and so on. The elements in insoluble residues are mainly in the form of microcline $(KAlSi_3O_8)$ and quartz (SiO_2). To further utilize these valuable elements in the residue (PS), especially the K element in microcline $(KAlSi_3O_8)$, the roasted calcination of $CaCl_2$ + PS in the presence of steam will be deployed. This steam-mediated high-temperature process shows very appealing advantages over current available processes used for potassium extraction from K-feldspar minerals: (i) no need to use a large volume of fresh water to extract the K element after high-temperature roasting, (ii) significant reduction of the external input of $CaCl_2$ as the H_3PO_4 production process will continuously produce the byproduct $(CaCl_2)$ during the acid leaching step, (iii) avoiding the separation of KCl out of the aqueous solution from conventional $CaCl_2$ + K-feldspar roasting,[16,17] and (iv) the produced HCl and KCl can be simultaneously and continuously moved out of the system through the flux of steam at ambient pressure during the reaction. From the energy cascade utilization and material recycling perspective, this proposed Cl^{-1} ion-based steam-mediated process is an essentially sustainable and environmental-friendly approach; it not only substantially tackles the hitherto problem of the integrated PR utilization but also paves a new way for processing the minerals that shares similar minerology features. The reports of this new process, to the best knowledge of authors, have never been published before.

2. EXPERIMENTS

2.1. Description of the Process with HCl Recovery and KCl Generation. Due to the complex mineral matrix of PR (obtained from the Xingfa group in Hubei Province, People's Republic of China), this work focuses on the investigation of the main elements such as K, Ca, and Si and their corresponding associated reactions. All experiments were repeated with three replica, and the experimental uncertainties were kept within ±5%. The characterization of PR used in this work is shown in Figure 1. The type of sedimentary rock is featured with (i) a relative lower level of P in $Ca_5(PO_4)_3F$ ($Ca_5(PO_4)_3F$ content less than 50 wt % in PR) and (ii) a relative higher level of impurities, that is, K and Ca. The X-ray fluorescence (XRF) results indicate that the percentages of three main compositions, namely, $Ca_5(PO_4)_3F$, $CaMg(CO_3)_2$, and SiO_2, are over 85 wt % in the PR (Figure 1A). The crystallite quartz, fluorapatite $(Ca_5(PO_4)_3F)$, and dolomite $(CaMg(CO_3)_2)$ are the main compositions in the crystallite matrix of PR (Figure 1B). The mineral often presents a dark-greenish color (Figure 1C). The scanning electron microscopy (SEM)−energy-dispersive X-ray spectroscopy (EDS) mapping (Figure S1) of PR also indicates its complexities with existence of trace elements such as S, Fe, Al, Mg, and so on. Once the PR is leached by HCl, the majority of P, Ca, and Mg elements comes into the leachate, and the characterization of the remaining acid-insoluble residue [phosphorous-rock slag (PS)] is shown in Figure 2.

The XRF results indicate that the percentages of three main compositions, namely, $KAlSi_3O_8$, SiO_2, and FeS_2, are over 90 wt % in the PS with trace amounts of elements, that is, Mg (0.6 wt %), P (0.3 wt %), and Ca (0.2 wt %), respectively (Figure 2A). The crystallite microcline $(KAlSi_3O_8)$, quartz (SiO_2), and pyrite (FeS_2) are the main composites in the crystallite matrix

of PS (Figure 2B). The color of PS becomes dark gray (Figure 2C). The SEM−EDS mapping (Figure 2D) of PS also indicates its complexities with existence of various elements such as K, Fe, Al, Si, and so on.

The filtrated and dried PS was then impregnated with $CaCl_2$ (precipitated from the leachate during the step of crystallization) at different ratios. The mixture was put in a ceramic boat reactor to react with steam at different temperatures (600−1000 °C). The experimental rig for this reaction is shown in Figure 3. The steam is quantitatively counted using a
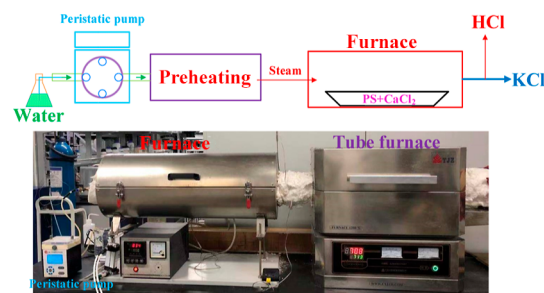
Figure 3. Schematic diagram and experimental setup of steam reaction for the coupled HCl recovery and the KCl generation, where PS refers to phosphorous slag.

peristatic pump, and the volume fed into the reaction zone is calculated using the ideal gas law (the experimental conditions were kept at high temperature and ambient pressure, where the use of the ideal gas law is appropriate)

$$PV = nRT \tag{1}$$

where P refers to the pressure of the operational condition (in this work, the operational pressure was kept at 1 atm), V is the volume of the gas (m^3), n refers to the mole of the gas (mole), R refers to the gas constant, and T refers to the operational temperature (K). Once the water was pumped into the preheating section, it was heated up and evaporated into vapor at the designated temperature. Then, the preheated steam (at a flow rate of 3 mL/min) was fed into the tube furnace to react with the mixture (PS + $CaCl_2$) at different temperatures. The outlet of the reactor was ducted to the heat exchanger to separate the condensed KCl (below its dew point) and HCl vapor. The concentration of Cl^{-1} in HCl vapor was determined by mercury nitrate titration at the outlet. The concentration of K^+ is measured by inductively coupled plasma−optical emission spectrometry (ICP-OES). After reaction, the residue in the ceramic boat reactor was taken out of the tube furnace for elementary mass balance calculations and subsequent characterization.

The total process of utilizing PR with the main mass flows (based on 100 g of PR) for simultaneous HCl and KCl regeneration is depicted in Figure 4. Apart from producing phosphorous acid (H_3PO_4), more than 90 wt % of K, Ca, and Si can be effectively high-value-converted into useful products, let alone the relative easiness in regenerating the acid (HCl, the consumption of hydrochloric acid is substantially reduced to 90 wt % less compared with the conventional leaching process, in which the acid is not regenerated). By recovering the acid through the process, it significantly reduces the amounts of external demands of the acid consumed for dissolving the PR and the production of H_3PO_4. For the convenience of study, in this work, we simply focus on the $CaCl_2$ + PS mixture and its
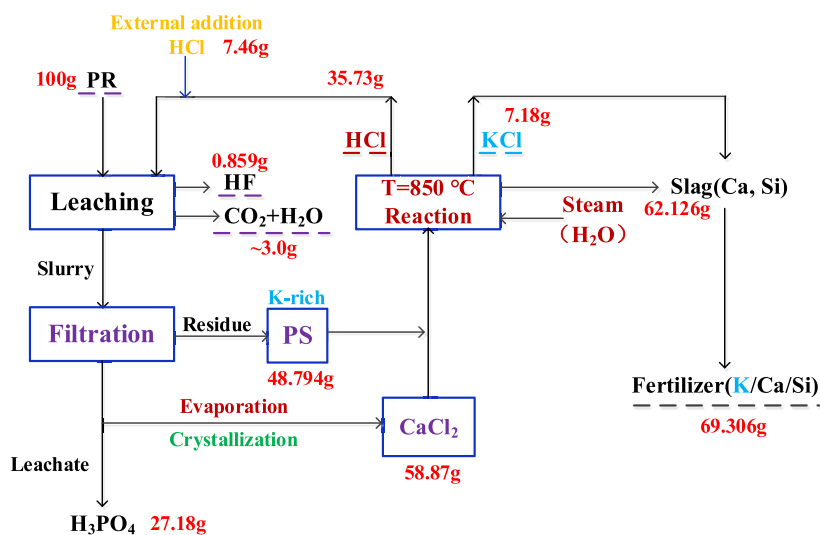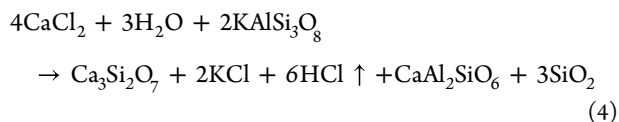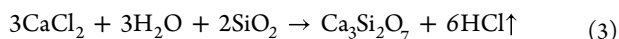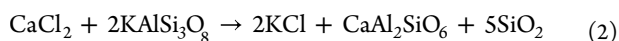
Figure 4. Process of the coupled HCl recovery and KCl generation using K-containing PR based on Ca-involved reactions. PS refers to phosphorous-rock slag.

corresponding reactions in the presence of the steam at high temperature.

2.2. Characterization. The characterization of samples includes X-ray diffraction (XRD) using an Empyrean PANalytical B.V. with 50 kV, SEM, and EDS using a ZEISS Sigma300 VP, a photoelectron spectrometer (XPS), Thermo-Fisher Scientific ESCALAB 250Xi, with parameters set at Al K α (source), 200 W (power), 500 μm (spot size), and 2.0×10^{-9} mbar (vacuum) with carbon (1s) as a calibration peak. The metal elements in solution were determined by ICP-OES (Optima 5300 DV, PerkinElmer, USA).

2.3. Thermodynamic Analysis of the Potential Reactions. In this work, the HSC chemistry 6 software (Outokumpu Technology) was used to perform a preliminary thermodynamic analysis of the potential reactions. The chemical potentials of these reactions were estimated at different temperatures at ambient pressure. To narrow down the scope of reaction selection, this work focuses on those existing mineral compositions in the PS matrix (Figure 2) and the main products after reaction (in both the solid residue and outlet vapor such as KCl and HCl). Therefore, the main possible reactions during HCl and KCl generation are illustrated below

$$CaCl_2 + 2KAlSi_3O_8 \rightarrow 2KCl + CaAl_2SiO_6 + 5SiO_2 \quad (2)$$

$$3CaCl_2 + 3H_2O + 2SiO_2 \rightarrow Ca_3Si_2O_7 + 6HCl\uparrow \quad (3)$$

$$4CaCl_2 + 3H_2O + 2KAlSi_3O_8$$
$$\rightarrow Ca_3Si_2O_7 + 2KCl + 6HCl \uparrow + CaAl_2SiO_6 + 3SiO_2 \quad (4)$$

Among these reactions, reaction 2 refers to the roasting mixture (PS + CaCl₂) in the absence of steam at high temperature, while reactions 3 and 4 refer to the reactions between the PS + CaCl₂ mixture and steam. The corresponding Gibbs free energies of these reactions were plotted and are shown in Figure 5. Among these three different reactions 2−4 at the investigated temperature range, the chemical potentials of reactions 3 and 4 fall into the spontaneous zone. This indicates that the absence of steam
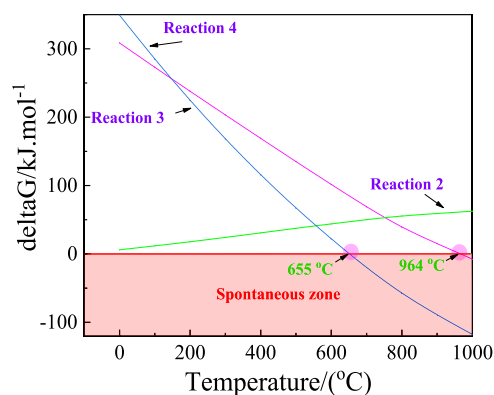

Figure 5. Thermodynamic analysis of potential reactions during the PS + CaCl₂ roasting with steam.

is thermodynamically unfavorable to the formation of KCl and HCl at high temperature. With regard to the temperature range, the lowest temperature for reaction 4 to occur is around 655 °C, while it is around 964 °C for reaction 3. This indicates that reaction 4 might predominantly occur at the investigated experimental conditions, while reaction 3 will step in once the system temperature reaches 964 °C. In addition, because of the feature of the experimental setup, it offers a transport advantage of continuous removal of the generated products, that is, HCl and KCl, out of the system by the influx of the steam, which will make reaction balance further skewing toward the generation of HCl and KCl (reactions 3 and 4). Therefore, from the above preliminary thermodynamic analysis, it is found that the introduction of steam to (PS + CaCl₂) plays a critical role during the formation of HCl and KCl. From the values of entropy and enthalpy of reactions 3 and 4,[18] the Gibbs free energy is calculated as follows

$$\Delta G = \Delta H - T\Delta S \quad (5)$$

where G refers to the Gibbs free energy (kJ mol⁻¹), H refers to the enthalpy (kJ mol⁻¹), and S refers to the entropy (kJ mol⁻¹). As reaction approaches equilibrium, the equilibrium constant is expressed as follows
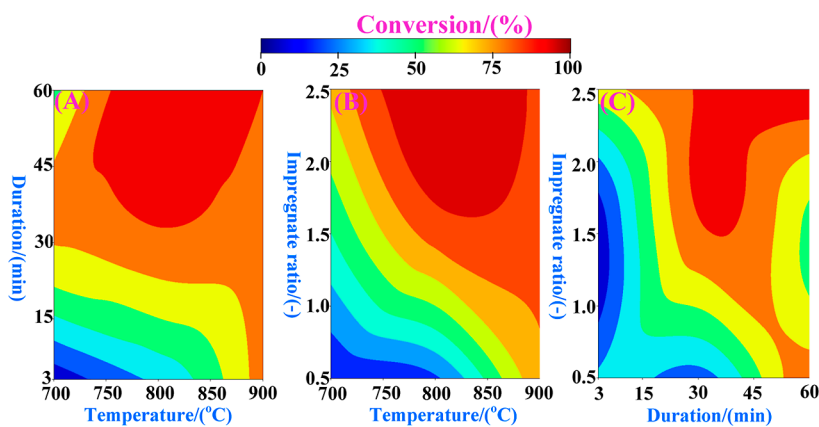
Figure 6. Optimization of operational conditions for KCl conversion using SML: (A) temperature versus duration for KCl conversion, (B) temperature versus impregnate ratio for KCl conversion, and (C) duration versus impregnate ratio for KCl conversion.

$$\ln K = -\frac{\Delta G}{RT} \qquad (6)$$

$$K = K_0 e^{E_a/RT} \qquad (7)$$

where K refers to the reaction constant, K_0 refers to the reaction constant under standard conditions, R refers to the gas constant (8.314 J mol^{-1} K^{-1}), and E_a refers to the activation energy (kJ mol^{-1}). The calculation of activation energies for reactions 3 and 4 is shown in Figure S2, with 150 (kJ mol^{-1}) for B and 208 (kJ mol^{-1}), respectively. These values generally fall into the range of activation energies of chemical reactions such as MnCl$_2$ + steam reactions.[19,20]

2.4. Kinetic Study of the Process. The reaction was carried out in a boat reactor heated using the tube furnace. By carefully controlling the amount of water using the peristatic pump, one can quantitatively estimate the amount of steam at the designated operational temperature. The reaction zone was maintained at different temperatures from 700 to 900 °C with the duration from 10 to 150 min. The obtained solid residue in the ceramic boat was grinded into powder, followed by mixed acid [hydrofluoric acid (HF) and nitric acid (HNO$_3$) by 1:1 volume ratio] leaching at a liquid-to-solid ratio of 10:1 for 30 min. The resultant slurry was finally filtered and oven-dried (105 °C). The K$^+$ content in the filtrate was measured by ICP-OES. The corresponding conversion (x) of KCl is calculated as follows

$$x = \frac{m_1\alpha - m_2\beta}{m_1\alpha} \times 100 \qquad (8)$$

where m_1 is the mass in the reactants, α is the K content in the PS (wt %), m_2 is the mass in the solid residue, and β is the K content in the solid residue (wt %).

2.5. Process Optimization Using the Supervised Machine Learning Approach. The preliminary experiment indicates that X$_1$, reaction temperature; X$_2$, reaction duration; and X$_3$, impregnate ratio (PS over CaCl$_2$) were critical during reaction (KCl conversion). Therefore, these three operational parameters were investigated to find out quantitative correlations with conversion (based on KCl conversion). In this work, 17 experimental conditions were used as training data set (Table S1). For neuron network construction, the activation functions in the neuron network architecture are one of the most important ones,[21,22] which are used to transform input (using the summed weighted approach) into the

activation of the node. In this work, the rectified linear activation function (ReLU) was used in the Tensorflow during supervised machine learning (SML) process to minimize the errors caused by the vanishing gradient.[11] The outcome of SML for the optimization are shown in Figure 6. With multiple objective functions by maximizing KCl conversion, the optimal conditions were achieved as X$_1$-850 °C, X$_2$-40 min, and X$_3$-2.5, respectively. The subsequent validation experiment conducted at this achieved optimal condition (X$_1$-850 °C, X$_2$-40 min, X$_3$-2.5) shows <±10% uncertainties, indicating a relatively good prediction from this SML algorithm.

2.6. Molecular Simulation Study. The total energy is calculated and expressed by assuming all ground-state properties to be functionals of the charge density[23]

$$E_t[\rho] = T[\rho] + U[\rho] + E_{XC}[\rho] \qquad (9)$$

where $E_t[\rho]$ is the total energy, $T[\rho]$ is the kinetic energy (non-interacting particles with density ρ), $U[\rho]$ refers to the classical electrostatic energy contributed from the Coulombic interactions, and $E_{XC}[\rho]$ refers to the exchange and correlation energies that contribute to the total energies. For the density function theory (DFT) calculation, the semi-empirical dispersion−correction schemes were used. The simulated annealing is deployed to locate a good approximation with the global minimum of a given function in a large search space.[24] The Metropolis Monte Carlo method is deployed to estimate the total energy of water steam adsorption on the model composites at ambient pressure and 1097 K. In this method, the sorbate structure is treated as rigid. Only rigid body translations and reorientations are incorporated during calculations.

3. RESULTS AND DISCUSSION

3.1. Kinetic Study. The kinetic profiles of reaction with and without steam at 800 °C are shown in Figure 7A. Obviously, the reaction in the absence of steam yields a poor performance in KCl conversion at the exit of the reactor. This agrees with the preliminary thermodynamic analysis of reaction 2. With the introduced steam, the reactions (reactions 3 and 4) toward the formation of products, either HCl or KCl or both, occur as a certain temperature threshold is reached. The kinetic profile of reaction with the steam and the morphology of solid residues and formed KCl are depicted in Figure 7B. Starting from PS, the color of the solid residue gradually changes from dark to gray as the reaction (eq 4) proceeds. In
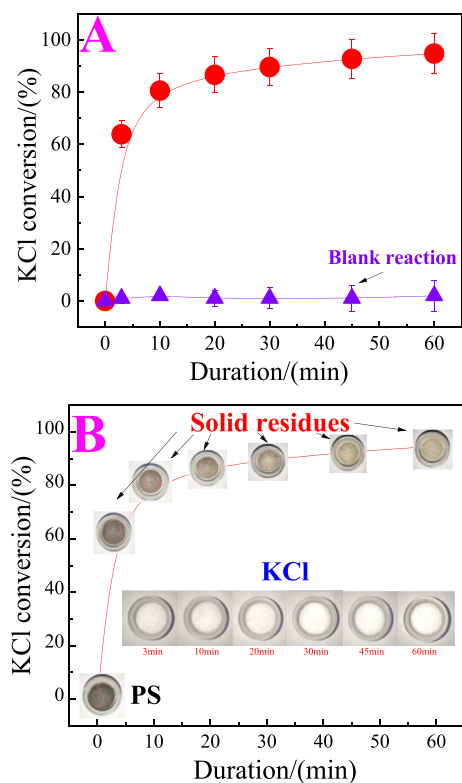
Figure 7. Kinetics of reactions: (A) KCl conversion of the blank reaction (no steam mediated) and KCl conversion with steam mediated at 800 °C and (B) steam-mediated kinetic profile of solid residues and the produced KCl at 800 °C, where PS refers to phosphorous slag and blank reaction refers to PS + CaCl$_2$ in the absence of steam at 800 °C.

addition, the KCl carried by the steam flux presents a very similar appearance with an increase of duration. More than 75% of K$^+$ ions are converted within the first 10 min, indicating that the reaction at 800 °C is kinetically favorable. Once the temperature reaches 800 °C, the chemical potential for reaction (eq 4) becomes favorable to the direction toward to the formation of KCl and HCl. Besides, the continuous removal of the products, that is, KCl and HCl, out of the reaction system will enhance the skewing reaction direction toward the formation of KCl and HCl. Therefore, both thermodynamic evidence and kinetic evidence suggest the feasibility and practicality of this proposed process for simultaneous HCl and KCl production in the presence of steam.

In this work, the shrinking core model (SCM) is used to estimate the conversion (on the KCl basis).[25,26] The reaction time (t) and the KCl conversion (x) can be expressed in the following form, which includes all the controlling steps

$$t = \frac{C_{S0}r}{3k_gC_{A0}}x + \frac{C_{S0}r}{3k_sC_{A0}}[1 - (1 - x)^{1/3}]$$
$$+ \frac{C_{S0}r^2}{6D_eC_{A0}}[1 - 3(1 - x)^{2/3} + 2(1 - x)] \quad (10)$$

where t is the reaction time (min), C_{S0} is the initial solid concentration (mol/L), C_{A0} is the initial concentration (mol/L), k_g is the gaseous diffusion constant factor (m^2/s), k_s is the surface reaction constant factor (m^2/s), and D_e is the effective diffusivity (this refers to diffusion of vapor KCl in steam at a

higher temperature, m/s). The modified correlation between the conversion and kinetic constant factor for the reaction is depicted as follows

$$x = \left(1 - \frac{k_c}{d^{0.6}}t\right)^{1/3} \quad (11)$$

$$k_c = k_{c0}e^{E_a/RT} \quad (12)$$

$$k_s = \frac{\rho_c}{M}\frac{k_cr^{0.4}}{2^{0.6}} \quad (13)$$

where k_c is the modified reaction rate constant (m$^{-0.6}$/s), d is the average diameter of the particle (in this work, the averaged particle size is around 23 μm and the particle size distribution of PS + CaCl$_2$ is shown in Figure S3), E_a is the activation energy (kJ/mol), R is the ideal gas constant (8.31 J/mol/K), T is the temperature of reaction (K), ρ_c is the density of the PS particle (kg/m^{-3}), M is the molecular mass of the reagent (kg/mol), and r is the average particle radius (m) with the following correlation

$$r = \frac{\rho_c}{M}\frac{k_cr^{0.4}}{2^{0.6}} \quad (14)$$

$$k_s = \frac{3}{\rho_cS} \quad (15)$$

where S refers to the surface area of the reagent (PS + CaCl$_2$); in this work, all particles in the ceramic boat reactor are assumed to be around 1.5 m^2/g. The conversion expression can be further reduced to a simpler expression if the overall rate is controlled by the surface reaction as follows

$$\frac{t}{\tau} = [1 - (1 - x)^{1/3}] \quad (16)$$

$$\tau = \frac{C_{s0}r}{k_sC_{A0}} \quad (17)$$

Then its derivative can be cast into the following

$$\frac{dx}{dt} = \frac{3(1 - x)^{2/3}}{\tau} \quad (18)$$

The conversion expression can be simplified into the following if the reaction is controlled by the diffusivity (transport control)

$$\frac{t}{\tau} = [1 - 3(1 - x)^{2/3} + 2(1 - x)] \quad (19)$$

$$\tau = \frac{C_{s0}r^2}{6D_eC_{A0}} \quad (20)$$

and its derivative can be achieved as

$$\frac{dx}{dt} = \frac{1}{2\tau}\frac{(1 - x)^{1/3}}{1 - (1 - x)^{1/3}} \quad (21)$$

The results of kinetics at three different temperatures (from 700 to 900 °C) are shown in Figure 8. Among different controlling steps (diffusion control, r^2 = 88%; reaction control, r^2 = 86%; and diffusion + reaction control, r^2 = 99%), the best fit curve of SCM (judging from the r square value) is achieved by considering all controlling steps (diffusion and chemical reaction). This indicates that the intrinsic kinetics and
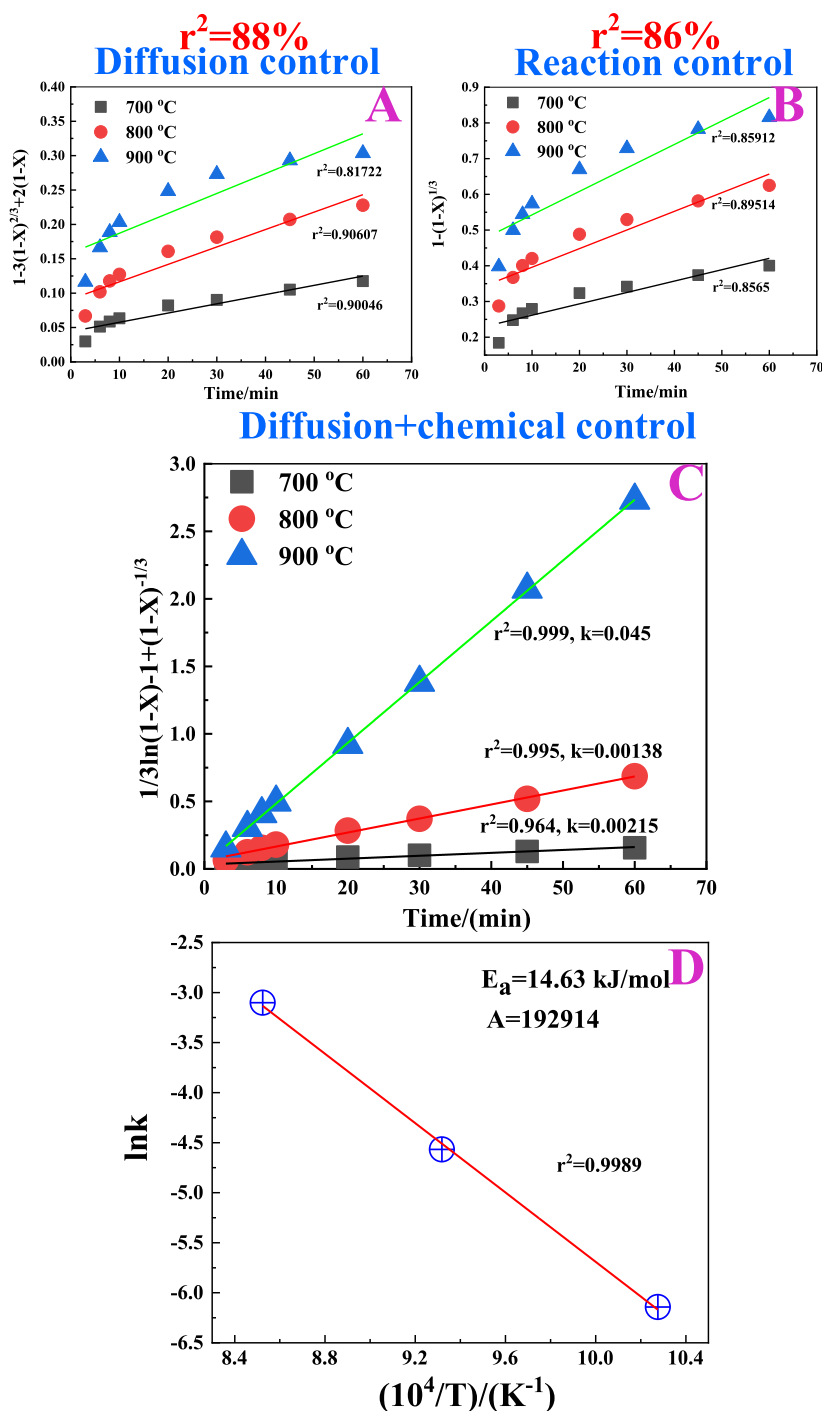
Figure 8. Kinetics of KCl conversion using SCM at different temperatures: (A) curve fitting using the diffusion control model, (B) curve fitting using the chemical control model, (C) curve fitting using the diffusion + chemical control model, and (D) activation energy estimation, where E_a refers to the activation energy and A refers to the pre-factor.

transport are both influential at the investigated experimental conditions. The corresponding activation energy (E_a) is around 14.63 (kJ/mol). In general, the magnitude of the activation energy for chemical reactions will be around 40−200 kJ/mol for roasting reactions between $CaCl_2$ and potassium sources such as K-feldspar in the absence of steam,[27,28] which generally agrees with the values calculated from theoretical thermodynamic analysis for the activation energies of the proposed potential reactions 3 and 4 (reaction 3, E_a = 150 kJ/mol; reaction 4, E_a = 208 kJ/mol). However, according to the

definition of the SCM, this type of model is used to describe the situation in which solid particles are consumed by either dissolution or reaction; as a result, the amount of material being consumed shrinks. Therefore, the activation energy obtained from SCM simply based on KCl conversion might not be able to completely represent the intrinsic kinetics of the reactions (in reactions 3 and 4, respectively). This indicates that the use of SCM might underestimate the activation energy of the reactions during the contact of the mixture (K-feldspar + $CaCl_2$) with steam at the investigated temperature range. The
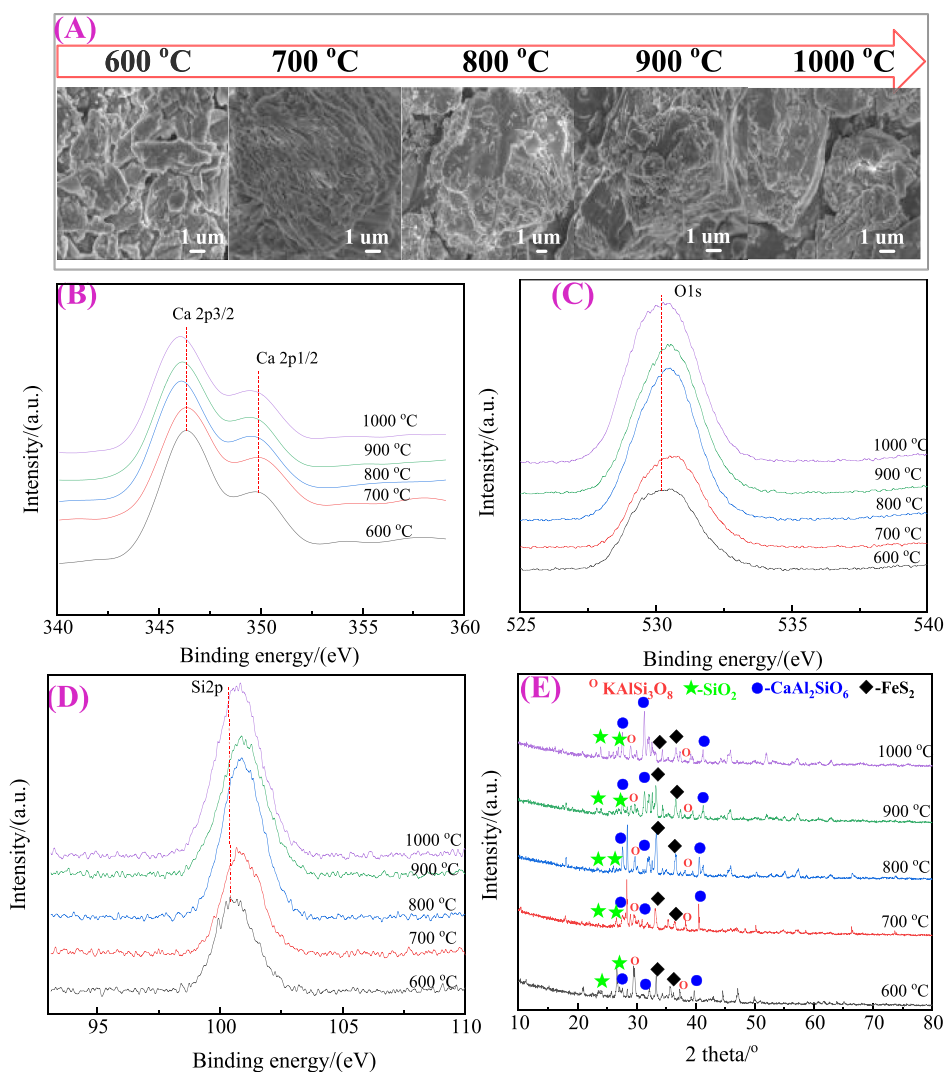
Figure 9. Characterization of solid residues at different temperatures: (A) SEM morphology, (B) XPS for Ca²⁺, (C) XPS for O 1s, (D) XPS for Si 2p, and (E) XRD. All other parameters were kept at the optimal condition (duration = 30 min, impregnate ratio = 2).

merit of using SCM lies in the quantitative identification of controlling dominant steps (diffusion, chemical reaction, or the combination) during reactions. For process intensification, some experimental conditions such as the relative smaller particle size of PS + CaCl₂ (Figure S3) and the involvement of high-temperature steam (continuously removing the produced products, i.e., HCl and KCl) might all contribute to further reduction of the value of the actual apparent activation energy of the reaction.[20,29] The improvement of these factors, that is, reducing particle size, increasing flows, and so on, will be helpful to the process intensification during the step of process scale-up.

3.2. Characterization of Solid Residues at Different Temperatures. Although various parameters affect the reaction, the reaction temperature is one of the most critical parameters that influence the reaction.[30,31] The characterization of the solid residues at different temperatures is shown in Figure 9. With an increase of reaction temperature, no substantial morphological differences are observed among all residues after reaction (Figure 9A). The XPS of Ca ($2p_{1/2}$ and $2p_{3/2}$), O 1s, and Si 2p is shown in Figure 9B−D, respectively. It is found that the binding energy of Ca $2p_{1/2}$ and Ca $2p_{3/2}$ (especially Ca $2p_{3/2}$) of the solid residue tends to shift toward

relatively lower binding energies with an increase of reaction temperature. This is associated with the broken ionic bond between Ca²⁺ and Cl⁻ (CaCl₂) and the formation of calcium aluminum silicate (CaAl₂SiO₆). The binding energies of both O 1s and Si 2p tend to shift to a relative higher energy with an increase of reaction temperature. The change from microcline (KAlSi₃O₈) to calcium aluminum silicate (CaAl₂SiO₆) and the formation of the Si-contained composites (in the form of Si−O connection) are both associated with the rearrangement of bindings between the oxygen atom and other atoms (i.e., Al, Ca) in the mineral matrix.[32,33]

A similar shifting pattern from Si 2p is observed, suggesting that more lattice silica atoms are found on the surface of the solid residue with an increase of temperature. The XRD spectra are shown in Figure 9E. The combined sharp and small peaks in each sample indicate the complexity of crystallite minerals in the solid residue.[34−36] With an increase of temperature, the intensity of the peaks from quartz becomes smaller. This indicates that the original crystallite structure of quartz in PS might be consumed because of reactions (i.e., reactions 3 and 4). The characteristic peaks of KAlSi₃O₈ experience a decrease, indicating the consumption of microcline as reaction proceeds. This orchestrates with the increased
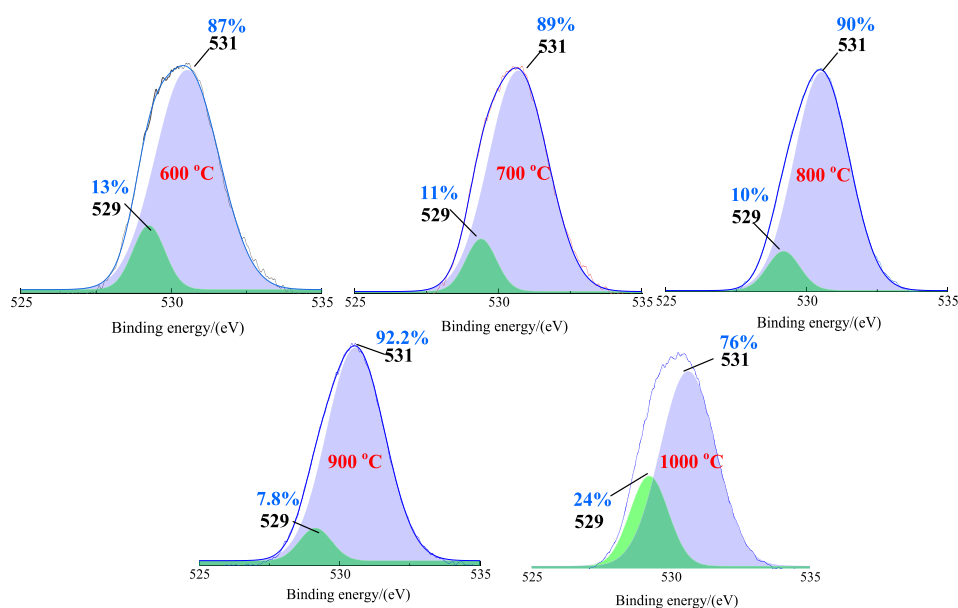
Figure 10. XPS peak splitting for O 1s for solid residues at different temperatures.
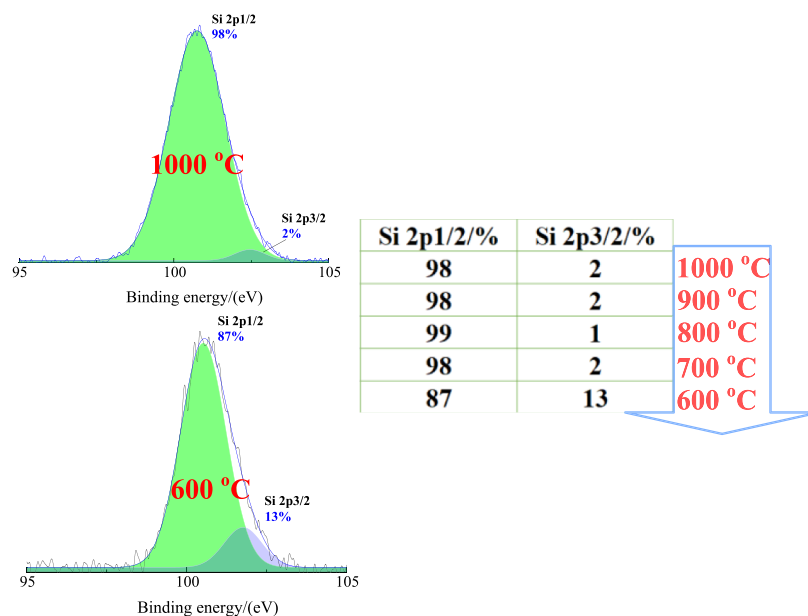

Figure 11. XPS peak splitting for Si of solid residues at different temperatures and the different peak area percentages by deconvolution.

intensity of the peaks for calcium aluminum silicate $(CaAl_2SiO_6)$ with an increase of temperature. Other impurities such as pyrite persistently exist in the solid residue with different intensities.[37]

To investigate the detailed binding energies of the formed oxidative minerals, the broad O 1s peak is split into two parts; the binding energy centers around 529 eV are associated with Ca–O, and the binding energy centers around 531 eV are associated with Al–O.[38,39] The main bands by deconvolution are shown in Figure 10. With an increase of reaction temperature, the binding energy of Al–O tends to gradually increase, while Ca–O experiences a decrease from 600 to 900 °C, indicating the gradual consumption of $CaCl_2$ and the formation of calcium aluminum silicate $(CaAl_2SiO_6)$ in the solid residue after reaction. As the reaction temperature reaches 1000 °C, the portion between 531 eV (Al–O) and 529

eV (Ca–O) experiences an appreciable transitional change. A relative increased portion of 529 eV (Ca–O) up to 24% and a decrease to 76% of 531 eV (Al–O) are observed. One of the reasons might be due to the start of other side reactions that lead to the formation of the new calcium and aluminum oxides. According to the preliminary thermodynamic analysis, reaction 3 will start to step into the spontaneous zone once the reaction temperature is over 946 °C (Figure 5), where new products such as rankinite $(Ca_3Si_2O_7)$ start to form and the corresponding O 1s binding energy will change accordingly (Figure 11).

The XPS spectra of Si were also recorded to ascertain the compositions associated with silica in the solid residues. Although spectra displayed the broad Si band, they also revealed the presence of valence around the Si atom arising from bonding with oxygen. Through the deconvolution, two
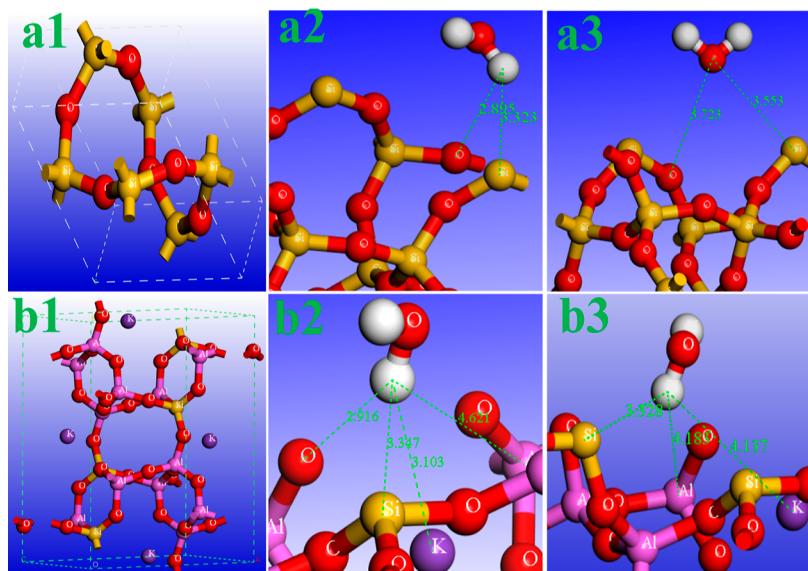
Figure 12. Molecular simulation for water adsorption on microcline: (a1) crystal structure of quartz, (a2) water adsorption configuration on quartz with the oxygen bond distance, (a3) water adsorption configuration on quartz with the hydrogen bond distance, (b1) crystallite structure of microcline, (b2) water adsorption configuration on microcline with the hydrogen bond distance, and (b3) water adsorption configuration on microcline with a larger bond distance.

bands at 102.5 eV (Si−O) and 103.4 eV (O−Si−O) are achieved, which correspond to Si $2p_{1/2}$ and Si $2p_{3/2}$, respectively.[40] With an increase of temperature over 600 °C, the majority of the valence around the Si atom is in the form of Si $2p_{1/2}$ (Si−O) with some valence around Si existing in the form of O−Si−O and the substoichiometric SiOx.[41] This also agrees with O 1s spectra; that is, the binding energy of the oxygen atom for O−Si−O locating at 532.5 eV is not appreciably observed. Therefore, the valence that the Si atom binds with other atoms is the most through Si−O. In other words, the Si atom exists mostly in the complex composite's clusters (i.e., $CaAl_2SiO_6$, $Ca_3Si_2O_7$, etc.) rather than in the pure quartz (SiO_2) crystal matrix, which agrees reasonably well with the postulated reactions (reactions B and C). This result also agrees with the XRD spectra (Figure 9E) analysis that the intensity of quartz in the solid residue at a higher temperature does not appreciably increase.

3.3. Preliminary Reaction Mechanism Discussion. As steam plays a critical role during reaction, it is necessary to investigate the interactions between the steam molecule and the key minerals in the PS + $CaCl_2$ matrix. Since the adsorption is the first step prior to the reaction, the total energies of the adsorption between the water molecule and the microcline, silica, and $CaCl_2$ composites might shed some insightful light on the reaction mechanism. As mineralogy of PS is quite complicated, we only focus on the main mineral composites (shown from PS characterization data in Figure 2) such as microcline (the crystal 024 plane was chosen for adsorption using the lattice parameters a = 24.97, b = 9.31, c = 8.57 Å and angles α = 90, β = 81.1, γ = 90),[42] quartz (the crystal −100 plane was chosen for adsorption using the lattice parameters a = 4.913, b = 4.913, c = 5.4052 Å and angles: α = 90, β = 90, γ = 120),[43] and $CaCl_2$ (the crystal 010 plane was chosen for adsorption using the lattice parameters a = 15.25, b = 18.65, c = 3.64 Å and angles: α = 90, β = 90, γ = 90),[44] respectively.

To obtain some detailed information about the adsorption of water on the model compounds, the density functional

theory (DFT) approach is employed and the results of water adsorption on quartz (SiO_2) and microcline ($KAlSi_3O_8$) are summarized in Figure 12 (12_a1, the crystallite structure of SiO_2; 12_a2 and 12_a3, different adsorption conformations on SiO_2 with different bond distances; 12_b1, the crystallite structure of microcline; 12_b2 and 12_b3, different adsorption conformations on $KAlSi_3O_8$ with different bond distances). Regarding the water adsorption on SiO_2, among these two adsorption conformations, the water (H−O−H) adsorption energy is appreciably smaller in position 1 (Figure 12_a2, adsorption energy: −0.87 eV) than that in position 2 (Figure 12_a3, adsorption energy: −0.82 eV). The corresponding bond distances between the H atom from H_2O and the O/Si atoms (H−O−H to O−Si: 2.895 Å, H−O−H to Si−O: 3.323 Å) tend to be shorter than that of the O atom from H_2O and O/Si−SiO_2 atoms (H_2−O to O: 3.723 Å, H_2−O to Si: 3.553 Å) due to the stronger adsorption energy. Therefore, the conformation of water with the H atom facing toward the surface of SiO_2 is considered to be most likely a steam conformation during reaction. In addition, combined with XPS analysis results, the existence of Si $2p_{1/2}$ atoms will contribute to the polarization of water molecules at a high temperature, which might facilitate the conformation of water molecules shown in Figure 12_a2. For water adsorption on microcline, it is more complicated due to the complexity of crystallite microcline (Figure 12_b1). The conformation of water is more likely to be the one shown in Figure 12_b2 with the bond distance (between the H atom from water and atoms from the microcline structure) varying from close to far (H−O 2.916 Å, H−K 3.103 Å, H−Si 3.347 Å, and H−Al 4.621 Å, respectively). The corresponding adsorption energies of conformation 1 (Figure 12_b2, adsorption energy: −0.19 eV) are smaller than that of configuration 2 (Figure 12_b3, adsorption energy: −0.13 eV). The total energy of water molecules adsorbed on different composites using the Monte Carlo approach is shown in Figure 13. At the simulated condition (T = 1073 K and P = 1 atm), the energy barrier for steam molecules to approach the surface of microcline is much
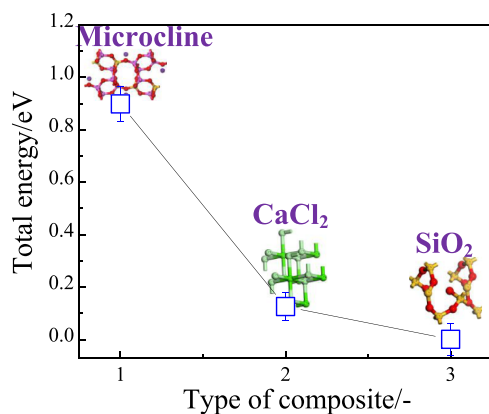
Figure 13. Total energy of water adsorption on the different model composites at 1073 K (1 atm) using the Monte Carlo approach, where 1 refers to microcline ($KAlSi_3O_8$), 2 refers to $CaCl_2$, and 3 refers to SiO_2.
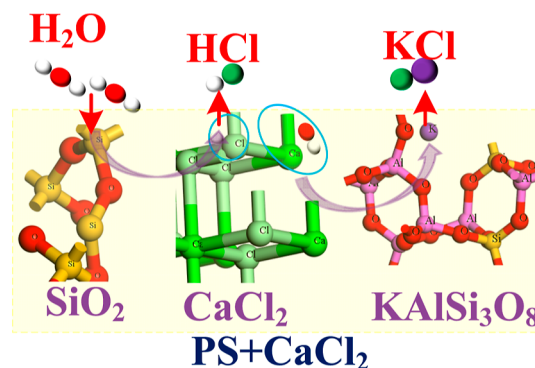

Figure 14. Schematic diagram of the reaction route of steam-mediated HCl and KCl formation reaction, where PS refers to phosphorous-rock slag.

higher than that of $CaCl_2$ and SiO_2. The energy barrier of SiO_2 is the lowest, indicating that it is more favorable for the steam molecule to adsorb on the surface of SiO_2. In addition, the preliminary experiment and thermodynamic analysis also show that the reaction between the $CaCl_2$ and H_2O cannot proceed if it is in the absence of SiO_2, even when the temperature is over 1000 °C (delta G = 6 kcal/mol). With existence of SiO_2 (one of the acid-insoluble residues in the PS residue) and the presence of steam, $CaCl_2$ becomes reactive and the formation of HCl and KCl begins to proceed at the experimental condition. Therefore, apart from introducing the steam, the existence of Si-O_x also significantly facilitates changing PS into KCl and HCl, respectively.

With all the above-mentioned information, the reaction route might be postulated as follows: (i) starting from the adsorption of steam molecules on the surface of SiO_2 with defects, followed by the spill over the polarized H−OH water molecule toward the surface of $CaCl_2$; (ii) the energized water will participate in breakdown of the crystallite structure of $CaCl_2$ (also indicated from Ca $2p_{3/2}$ shifting to a lower binding energy shown in Figure 9B), leaving the chloride ions (Cl^{-1}) out of the $CaCl_2$ matrix, which results in the formation of volatile HCl; iii) replacing the K^+ with Ca^{2+} cations in the microcline matrix with the assistance of the HCl at high temperature (as indicated from Figure 12_b1, the crystallite structure of microcline, K is much more loosely coalited with the Si−Al−O complex structure), resulting in the formation of KCl; and (iv) finally, the formed Ca−Si−Al−O composite will rearrange into the composite with the minimum chemical potential as it cools down (the products suggested by reactions 3 and 4 from thermodynamic analysis). The schematic diagram of the possible reaction route is summarized in Figure 14. Obviously, this postulated route is a quite simplified reaction pathway; it is believed that there will be more possible side reactions in the real scenario.

4. CONCLUSIONS

A clean process based on the steam-mediated reactions for the simultaneous HCl and KCl production using potassium (K)-containing phosphorous-rock slag (PS) as a precursor is proposed. The generation of both liquid products (H_3PO_4 and $CaCl_2$) and solid residues (PS rich in elements, i.e., K, Al, Si, etc.) in the form of microcline-$KAlSi_3O_8$ and quartz-SiO_2 was

achieved. The optimal conditions were achieved (X_1-850 °C, X_2-40 min, X_3-2.5) using the SML approach. Thermodynamic analysis and molecular simulation indicate that the presence of both steam and SiO_2 in the (PS + $CaCl_2$) matrix plays critical roles during the formation of HCl and KCl at high temperature. The SCM suggests that both the intrinsic kinetics and transport (diffusion) are influential at the investigated conditions, and the corresponding activation energy of E_a = 14.63 kJ/mol is obtained. The potential reaction pathway based upon experimental characterization and theoretical simulation is also postulated..

■ ASSOCIATED CONTENT

ⓢ Supporting Information

The Supporting Information is available free of charge at https://pubs.acs.org/doi/10.1021/acsomega.2c02362.

> Characterization of PR using SEM−EDS elementary mapping, activation energy estimation, particle size distribution of the PS + $CaCl_2$ mixture, and training data set for optimization using the SML approach (PDF)

■ AUTHOR INFORMATION

Corresponding Authors

  Gang Yang − *National Engineering Research Center of Green Recycling for Strategic Metal Resources, Institute of Process Engineering, Chinese Academy of Sciences, Beijing 100190, China*; Email: yanggang@ipe.ac.cn

  Yong Sun − *School of Engineering, Edith Cowan University, Joondalup, Western Australia 6027, Australia; Department of Chemical and Environmental Engineering, University of Nottingham Ningbo China, Ningbo 315100, China*; ⓞ orcid.org/0000-0002-4888-156X; Email: yong.sun@nottingham.edu.cn, y.sun@ecu.edu.au

Authors

  Yunshan Wang − *National Engineering Research Center of Green Recycling for Strategic Metal Resources, Institute of Process Engineering, Chinese Academy of Sciences, Beijing 100190, China*

  Lufang Shi − *Each Energy Technology (Suzhou) Co., Ltd., Suzhou 215021, China*

  Houli Li − *School of Chemical Engineering and Technology, Hebei University of Technology, Tianjin 300130, China*

  Yixiao Wang − *Key Laboratory of Carbonaceous Wastes Processing and Process Intensification of Zhejiang Province,*

University of Nottingham Ningbo China, Ningbo 315100, China

Zhiying Wang − School of Chemical Engineering and Technology, Hebei University of Technology, Tianjin 300130, China

Xuebin An − National Engineering Research Center of Green Recycling for Strategic Metal Resources, Institute of Process Engineering, Chinese Academy of Sciences, Beijing 100190, China

Mingzhu Tang − School of Chemical Engineering and Technology, Hebei University of Technology, Tianjin 300130, China

Jun He − Nottingham Ningbo China Beacons of Excellence Research and Innovation Institute, Ningbo 315021, China; Department of Chemical and Environmental Engineering, University of Nottingham Ningbo China, Ningbo 315100, China; orcid.org/0000-0001-8056-0347

Jing Hu − Key Laboratory of Carbonaceous Wastes Processing and Process Intensification of Zhejiang Province, University of Nottingham Ningbo China, Ningbo 315100, China

Complete contact information is available at:
https://pubs.acs.org/10.1021/acsomega.2c02362

Notes
The authors declare no competing financial interest.

■ REFERENCES

(1) Liu, L. H.; Ouyang, W.; Liu, H. B.; Zhu, J. Q.; Ma, Y. H.; Wu, Q. X.; Chen, J. R.; Zhang, D. Potential of paddy drainage optimization to water and food security in China. *Resour. Conserv. Recycl.* 2021, 171, 105624.
(2) Bassett, H. P. Process of Producing Alumina and Potash, US patent 1,404,083 A, 1922.
(3) Sun, Y.; Yang, G.; Zhang, J.-P.; Yao, M.-S. Clean Production of Corn Stover Pulp Using Koh+Nh4oh Solution and Its Kinetics during Delignification. *Chem. Ind. Chem. Eng. Q.* 2012, 18, 137−145.
(4) Sun, Y.; Wei, J.; Yao, M.-s.; Yang, G. Preparation of activated carbon from furfural production waste and its application for water pollutants removal and gas separation. *Asia-Pac. J. Chem. Eng.* 2012, 7, 547−554.
(5) Emsbo, P.; McLaughlin, P. I.; Breit, G. N.; du Bray, E. A.; Koenig, A. E. Rare earth elements in sedimentary phosphate deposits: Solution to the global REE crisis? *Gondwana Res.* 2015, 27, 776−785.
(6) Boumnijel, I.; Ben Amor, H.; Chtara, C. Effect of calcinated and activated perlite on improving efficiency of dihydrate process for phosphoric acid. *Int. J. Miner. Process.* 2013, 125, 112−117.

(7) Wang, Y.; Tang, M.; Yusuf, A.; Wang, Y.; Zhang, X.; Yang, G.; He, J.; Jin, H.; Sun, Y. Preparation of Catalyst from Phosphorous Rock Using an Improved Wet Process for Transesterification Reaction. *Ind. Eng. Chem. Res.* 2021, 60, 8094−8107.
(8) Lopez, F. A.; Tayibi, H.; Garcia-Diaz, I.; Alguacil, F. J. Thermal dehydration kinetics of phosphogypsum. *Mater. Constr.* 2015, 65, No. e061.
(9) Sun, Y.; Yang, G.; Zhang, L.; Sun, Z. Preparation of high performance H2S removal biochar by direct fluidized bed carbonization using potato peel waste. *Process Saf. Environ. Protect.* 2017, 107, 281−288.
(10) Koper, A.; Pralat, K.; Ciemnicka, J.; Buczkowska, K. Influence of the Calcination Temperature of Synthetic Gypsum on the Particle Size Distribution and Setting Time of Modified Building Materials. *Energies* 2020, 13, 5759.
(11) Li, H.; Hu, J.; Wang, Y.; An, X.; Tang, M.; Wang, Z.; Wang, Y.; Yang, G.; Bao, W.; Sun, Y. Utilization of phosphogypsum waste through a temperature swing recyclable acid process and its application for transesterification. *Process Saf. Environ. Protect.* 2021, 156, 295−303.
(12) Sun, Y.; Zhang, J. P.; Yang, G.; Li, Z. H. Study on the corn stover lignin oxidized by chlorine dioxide and modified by furfuryl alcohol. *Spectrosc. Spectr. Anal.* 2007, 27, 1997−2000.
(13) Zeng, L. L.; Bian, X.; Zhao, L.; Wang, Y. J.; Hong, Z. S. Effect of phosphogypsum on physiochemical and mechanical behaviour of cement stabilized dredged soil from Fuzhou, China. *Geomech. Energy Environ.* 2021, 25, 100195.
(14) Sun, Y.; Zhang, J.-P.; Yang, G.; Li, Z.-H. Production of activated carbon by H3PO4 activation treatment of corncob and its performance in removing nitrobenzene from water. *Environ. Prog.* 2007, 26, 78−85.
(15) Wu, P. *Phosphorous Acid Production from Wet Process*; Pressing House of Chemical Industry: Beijing, 1987; p 387.
(16) Haseli, P.; Majewski, P.; Christo, F. C.; Hammond, B.; Bruno, F. Thermochemical and Experimental Kinetic Analysis of Potassium Extraction from Ultrapotassic Syenite Using Molten Chloride Salts. *Ind. Eng. Chem. Res.* 2019, 58, 7397−7407.
(17) Samantray, J.; Anand, A.; Dash, B.; Ghosh, M. K.; Behera, A. K. Sustainable Process for the Extraction of Potassium from Feldspar Using Eggshell Powder. *ACS Omega* 2020, 5, 14990−14998.
(18) Green, D. W.; Southard, M. Z. *Perry's Chemical Engineers' Handbook*, 9th ed.; McGraw Hill: New York, 2018.
(19) Bischoff, J. L.; Rosenbauer, R. J.; Fournier, R. O. The generation of HCl in the system CaCl2-H2O: Vapor-liquid relations from 380-500 degrees C. *Geochim. Cosmochim. Acta* 1996, 60, 7−16.
(20) Yang, G.; Sun, Y.; Zhang, J.; Li, Z.; Wang, Y. Clean production of chlorine from hydrogen chloride with Mn-compound as intermediate. *Chin. J. Chem. Eng.* 2015, 23, 435−440.
(21) Sun, Y.; Yang, G.; Wen, C.; Zhang, L.; Sun, Z. Artificial neural networks with response surface methodology for optimization of selective CO2 hydrogenation using K-promoted iron catalyst in a microchannel reactor. *J. CO2 Util.* 2018, 24, 10−21.
(22) Wang, Y.; Hu, J.; Zhang, X.; Yusuf, A.; Qi, B.; Jin, H.; Liu, Y.; He, J.; Wang, Y.; Yang, G.; Sun, Y. Kinetic Study of Product Distribution Using Various Data-Driven and Statistical Models for Fischer−Tropsch Synthesis. *ACS Omega* 2021, 6, 27183−27199.
(23) Frenkel, D.; Smit, B. *Understanding Molecular Simulation: From Algorithms to Applications*; Academic Press: San Diego, 2002.
(24) Guillot, J.; Restrepo-Leal, D.; Robles-Algarin, C.; Oliveros, I. Search for Global Maxima in Multimodal Functions by Applying Numerical Optimization Algorithms: A Comparison between Golden Section and Simulated Annealing. *Computation* 2019, 7, 43.
(25) Sun, Y.; Wang, Y. X.; He, J.; Yusuf, A.; Wang, Y. S.; Yang, G.; Xiao, X. Comprehensive kinetic model for acetylene pretreated mesoporous silica supported bimetallic Co-Ni catalyst during Fischer-Trospch synthesis. *Chem. Eng. Sci.* 2021, 246, 116828−116844.
(26) Sun, Y.; Sage, V.; Sun, Z. An enhanced process of using direct fluidized bed calcination of shrimp shell for biodiesel catalyst preparation. *Chem. Eng. Res. Des.* 2017, 126, 142−152.

(27) Yang, G.; Li, Z.; Zhang, Y. Dehydration of tetrahydrate potassium pentaborate in fluidized bed. *Chem. Eng. Process.* **2005**, *44*, 1216−1220.

(28) Stamnore, B. R.; Gilot, P. Review-calcination and carbonation of limestone during thermal cycling for CO2 sequestration. *Fuel Process. Technol.* **2005**, *86*, 1707−1743.

(29) Türk, T.; Üçerler, Z.; Burat, F. .; Bulut, G.; Kangal, M. O. Extraction of Potassium from Feldspar by Roasting with CaCl2 Obtained from the Acidic Leaching of Wollastonite-Calcite Ore. *Minerals* **2021**, *11*, 1369.

(30) Wang, Y.; Tang, M.; Ling, J.; Wang, Y.; Liu, Y.; Jin, H.; He, J.; Sun, Y. Modeling biohydrogen production using different data driven approaches. *Int. J. Hydrogen Energy* **2021**, *46*, 29822−29833.

(31) Fogler, H. S. *Elements of Chemical Reaction Engineering*; Prentice-Hall: New Jersey, 2004.

(32) Hameed, A.; Raja, P.; Ali, M.; Upreti, N.; Kumar, N.; Tripathi, J. K.; Srivastava, P. Micromorphology, clay mineralogy, and geochemistry of calcic-soils from western Thar Desert: Implications for origin of palygorskite and southwestern monsoonal fluctuations over the last 30 ka. *Catena* **2018**, *163*, 378−398.

(33) Yanzhong, W.; Nianmin, Z.; Xu, C.; Yingchang, C.; Guanghui, Y.; Gluyas, J. G.; Miruo, L. Geologic CO2 storage in arkosic sandstones with CaCl2-rich formation water. *Chem Geol.* **2020**, *558*, 119867.

(34) Yuan, B.; Li, C.; Liang, B.; Lü, L.; Yue, H.; Sheng, H.; Ye, L.; Xie, H. Extraction of potassium from K-feldspar via the CaCl2 calcination route. *Chin. J. Chem. Eng.* **2015**, *23*, 1557−1564.

(35) Kalita, J. M.; Chithambo, M. L. Structural, compositional and thermoluminescence properties of microcline (KAlSi 3 O 8). *J. Lumin.* **2020**, *224*, 117320.

(36) Serdengecti, M. T.; Basturkcu, H.; Burat, F.; Kangal, M. O. The Correlation of Roasting Conditions in Selective Potassium Extraction from K-Feldspar Ore. *Minerals* **2019**, *9*, 109.

(37) Pourghahramani, P.; Akhgar, B. N. Characterization of structural changes of mechanically activated natural pyrite using XRD line profile analysis. *Int. J. Miner. Process.* **2015**, *134*, 23−28.

(38) Sun, C.; Zeng, R.; Zhang, J.; Qiu, Z.-J.; Wu, D. Effects of UV-Ozone Treatment on Sensing Behaviours of EGFETs with Al2O3 Sensing Film. *Materials* **2017**, *10*, 1432.

(39) Cui, Y.; Huang, K.; Nilius, N.; Freund, H.-J. Charge competition with oxygen molecules determines the growth of gold particles on doped CaO films. *Faraday Discuss.* **2013**, *162*, 153−163.

(40) Bywalez, R.; Karacuban, H.; Nienhaus, H.; Schulz, C.; Wiggers, H. Stabilization of mid-sized silicon nanoparticles by functionalization with acrylic acid. *Nanoscale Res. Lett.* **2012**, *7*, 76.

(41) Zeng, S.; Feng, W.; Peng, S.; Teng, Z.; Chen, C.; Zhang, H.; Peng, S. Dual-functional SiOC ceramics coating modified carbon fibers with enhanced microwave absorption performance. *RSC Adv.* **2019**, *9*, 30685−30692.

(42) Ren, Y.; Zhao, X.; Hagley, E. W.; Deng, L. Ambient-condition growth of high-pressure phase centrosymmetric crystalline KDP microstructures for optical second harmonic generation. *Sci Adv.* **2016**, *2*, No. e1600404.

(43) Tahiri, N.; Khouchaf, L.; Elaatmani, M.; Louarn, G.; Zegzouti, A.; Daoud, M. Study of the thermal treatment of SiO2 aggregate. *IOP Conf. Ser.: Mater. Sci. Eng.* **2014**, *62*, 012002.

(44) Moreira, J. C.; Santa, R. A. A. B.; Nones, J.; Riella, H. G. Synthesis of Zeolite 4a for Obtaining Zeolite 5a by Ionic Exchange for Full Utilization of Waste from Paper Industry. *Braz. J. Chem. Eng.* **2018**, *35*, 623−630.